Backscatter-to-Extinction Ratios in the Top Layers of Tropical Mesoscale Convective Systems and in Isolated Cirrus from LITE Observations

C. M. R. PLATT*

CSIRO Division of Atmospheric Research, Aspendale, Victoria, Australia

D. M. WINKER

NASA/Langley Research Center, Hampton, Virginia

M. A. VAUGHAN

Science Applications International Corporation, Hampton, Virginia

S. D. MILLER

Department of Atmospheric Science, Colorado State University, Fort Collins, Colorado

(Manuscript received 3 November 1997, in final form 2 November 1998)

ABSTRACT

Cloud-integrated attenuated backscatter from observations with the Lidar In-Space Technology Experiment (LITE) was studied over a range of cirrus clouds capping some extensive mesoscale convective systems (MCSs) in the Tropical West Pacific. The integrated backscatter when the cloud is completely attenuating, and when corrected for multiple scattering, is a measure of the cloud particle backscatter phase function.

Four different cases of MCS were studied. The first was very large, very intense, and fully attenuating, with cloud tops extending to 17 km and a maximum lidar pulse penetration of about 3 km. It also exhibited the highest integrated attenuated isotropic backscatter, with values in the 532-nm channel of up to 2.5 near the center of the system, falling to 0.6 near the edges. The second MCS had cloud tops that extended to 14.8 km. Although MCS2 was almost fully attenuating, the pulse penetration into the cloud was up to 7 km and the MCS2 had a more diffuse appearance than MCS1. The integrated backscatter values were much lower in this system but with some systematic variations between 0.44 and 0.75. The third MCS was Typhoon Melissa. Values of integrated backscatter in this case varied from 1.64 near the eye of the typhoon to between 0.44 and 1.0 in the areas of typhoon outflow and in the 532-nm channel. Mean pulse penetration through the cloud top was 2–3 km, the lowest penetration of any of the systems. The fourth MCS consisted of a region of outflow from Typhoon Melissa. The cloud was semitransparent for more than half of the image time. During that time, maximum cloud depth was about 7 km. The integrated backscatter varied from about 0.38 to 0.63 in the 532-nm channel when the cloud was fully attenuating.

In some isolated cirrus between the main systems, a plot of integrated backscatter against one minus the two-way transmittance gave a linear dependence with a maximum value of 0.35 when the clouds were fully attenuating. The effective backscatter-to-extinction ratios, when allowing for different multiple-scattering factors from space, were often within the range of those observed with ground-based lidar. Exceptions occurred near the centers of the most intense convection, where values were measured that were considerably higher than those in cirrus observed from the surface. In this case, the values were more compatible with theoretical values for perfectly formed hexagonal columns or plates. The large range in theoretically calculated backscatter-to-extinction ratio and integrated multiple-scattering factor precluded a closer interpretation in terms of cloud microphysics.

1. Introduction

It is now well understood that a knowledge of the heat budget of the tropical atmosphere is crucial to our understanding of the earth's climate and likely changes to that climate. This need is particularly true of the western reaches of the tropical Pacific Ocean, known also as the Warm Pool, where sea surface temperatures

* Current affiliation: Department of Atmospheric Science, Colorado State University, Fort Collins, Colorado.

Corresponding author address: Dr. C. Martin R. Platt, Dept. of Atmospheric Science, Colorado State University, Fort Collins, CO 80523.
E-mail: martin@reef.atmos.colostate.edu

are typically 30°C or warmer. This region is known also as the ''boilerhouse'' of the atmosphere because of a penchant there for the formation of deep convection that leads to the development of tropical mesoscale convective systems (MCSs) and even typhoons.

Tropical MCSs usually are identifiable in satellite radiance images through the large areas of cirrus that spread out from the convective storms and maintain themselves for considerable time (Webster and Stephens 1980). These large cloud systems are very important radiatively because they can possess a high albedo and they also radiate back to space in the infrared at very cold temperatures. These two radiation streams can balance out fairly closely at times, but also can cause considerable atmospheric column cooling or heating. The net radiative effects at the top of the atmosphere have been studied through the use of satellite radiance data, but it is not possible to retrieve column heating from such data. Recent simulations using cumulus cloud models have indicated that the greatest radiative effects may emanate from large-scale cooling at the tops of the MCSs (e.g., Miller and Frank 1993; Tao et al. 1996). Particularly relevant in that context is the cloud microphysics in the upper reaches of the convective clouds where radiative heating or cooling generally occurs.

Knollenberg et al. (1993), hereinafter referred to as KN, observed high number densities of small crystals near the tops of tropical storms around northern Australia. Wong et al. (1993) made observations in one tropical cloud cluster. Heymsfield and McFarquhar (1996) and McFarquhar and Heymsfield (1996) identified a significant small-particle mode in tropical cirrus, particularly near the tropopause. The presence of this small–ice crystal mode will affect the relationship between cloud optical depths and cloud ice water contents. Such information is needed to predict more realistic solar and infrared radiation flows in deep convection.

This paper examines the measured effective backscatter-to-extinction ratio (modified by the multiple-scattering factor) and its variation with cloud type in cold ice clouds. The deduced values are compared with those obtained from ground-based lidar and radiometry and from theoretical models of scatter. The well-established technique of using the integrated attenuated backscatter to obtain values of cloud particle backscatter-to-extinction ratio has been used in extensive studies of cirrus with ground-based lidar and radiometry (Platt et al. 1987, 1998). Values were found by these authors to increase systematically with temperature over a range from $-80°$ to $-20°$C. Observations were made at equatorial, tropical, and midlatitude sites. The observed temperature variation is considered to be due to a corresponding variation in cloud microphysics. The Lidar In-Space Technology Experiment (LITE) provided the opportunity to apply the technique to cirrus layers that cap large MCSs. Such layers are not visible to ground-based lidar but are encountered first at the top of the troposphere by space lidar or high-flying aircraft lidar platforms such as the ER-2. Some observations over the tops of convective storms were made previously from an aircraft by Spinhirne et al. (1982, 1983) although their data were not analyzed to give integrated backscatter. However, they form a useful first comparison with space lidar. There are also extensive aircraft lidar data on cirrus backscatter from the Central Equatorial Pacific Experiment (CEPEX) and Tropical Ocean and Global Atmosphere Coupled Ocean–Atmosphere Response Experiment (TOGA COARE) programs (e.g., Jensen et al. 1996). It is hoped to use these data for comparisons with the LITE data.

TABLE 1. LITE sampling parameters.

Parameter	Resolution
Vertical sampling	15 m
Horizontal distance between spot centers	740 m
Lidar receiver spot size at the surface (for a telescope receiver aperture of 1.1 mrad)	250 m

This article describes the techniques used to analyze some LITE backscatter data obtained from the top layers of several MCSs in the tropical western Pacific (TWP). Two of these MCSs were made up of parts of a typhoon, Melissa, in two stages of its development. Altogether, the cirrus clouds that were observed covered extensive regions of young, vigorous convective areas; some other broad areas of aging cirrus; and some isolated cirrus existing outside the MCSs. The latter two systems gave a range of effective backscatter-to-extinction ratios that were not too different from ground-based values. On the other hand, some areas with remarkably large values also were retrieved and were quite unlike anything that had been observed from the surface. Section 2 of this article gives a brief description of the LITE mission; section 3 describes the theory of the method; section 4 gives a description of the various case studies; section 5 describes the analysis of the data; section 6 gives a discussion of the results; and section 7 gives a summary and conclusions.

2. Experimental: The LITE mission

The LITE was flown aboard Space Shuttle *Discovery* from 9–19 September 1994. Scientific data were obtained for the allotted total of 53 h during that time. The shuttle flew in a 57° inclined orbit and was launched such that descending orbits occurred during nighttime and ascending orbits during daytime. The LITE experiment, lidar hardware, and system characteristics have been described fully elsewhere (e.g., Couch et al. 1991; McCormick et al. 1993; Winker et al. 1996). The LITE sampling parameters are listed in Table 1.

Data were obtained from several of the orbits that crossed the TWP for a priority project to obtain information on the characteristics of Warm Pool clouds. Orbits used in this study are listed in Table 2 together with the latitude regions and MCSs studied. LITE was point-

TABLE 2. Orbits and lat–long ranges of cirrus systems.

Target	Orbit No.	Orbit type*	Lat range	Long range
MCS1	13	D	10.7°–7.8°N	150.5°–152.0°E
MCS2	13	D	2.2°–7.9°S	158.0°–161.2°E
Isolated cirrus	13	D	7.1°–3.0°N	152.6°–155.0°E
MCS3	85	A	13.7°–23.7°N	156.5°–161.1°E
MCS4	117	A	27.0°–40.0°N	158.8°–171.6°E

*D = Descending nighttime orbit, A = Ascending daytime orbit.

ed toward the earth at an angle of about 5° to the nadir so that the lidar profiles cut a two-dimensional swath through the atmosphere. The off-nadir angle was chosen to minimize potentially intense specular reflection effects from water surfaces and from ice clouds composed of horizontal ice plates—reflections that could damage the telescope optical detectors. The telescope apertures employed were 1.1 mrad for daytime observations and 3.5 mrad at night.

The data were acquired in two forms. First, the ''quicklook'' data comprised 100-shot sequential averages and were available in near real time. Second, single-shot high-rate data were transmitted to the ground station and stored for later analysis.

3. Theory

a. Backscatter-to-extinction ratio and attenuated integrated backscatter

As stated previously, there is now a well-established method for retrieving cloud particle backscatter-to-extinction ratio k from lidar and radiometric data (e.g., Platt et al. 1987, 1998). The isotropic quantity k is numerically equal to the cloud particle backscatter phase function $P(\pi)$, which, in turn, is sensitive to the ice crystal habit. Now, k is defined by

$$k = B_c(\pi)/\sigma_c, \tag{1}$$

where $B_c(\pi)$ is an isotropic backscatter coefficient and σ_c is an extinction coefficient. Many authors define the backscatter coefficient in units of sr^{-1} and use the so-called ''lidar ratio,'' which is equal to $4\pi/k$ sr. In this paper, in order to be consistent with Platt et al. (1998) and earlier papers, we use the isotropic quantities.

Platt (1973) demonstrated that k could be retrieved from the cloud-integrated attenuated isotropic backscatter $\gamma'(\pi)$ when the cloud was fully attenuating. An equation relating the quantity $\gamma'(\pi)$ to the cloud optical depth δ_c for a semitransparent cloud can be derived (Platt 1979, 1981)

$$\gamma'(\pi) = \frac{k}{2\overline{\eta}}\{1 - \exp[-2\eta(z_t, z_b)\delta_c(z_t, z_b)]\}, \tag{2}$$

where $\eta(z_t, z_b)$ is a factor that describes the fractional decrease in observed effective optical depth $\delta(z_t, z_b)$ due to multiple scattering between cloud top z_t (for space lidar) and cloud base z_b and $\overline{\eta}$ is an effective multiple-scatter factor in the term $k/(2\overline{\eta})$ when the optical depth becomes large (Platt 1979, 1981). In this formulation, the values of $\overline{\eta}$ and $\eta(z_t, z_b)$ in (2) are not equal unless the multiple-scattering factor is constant throughout cloud depth. Otherwise, $\eta(z_t, z_b)$ varies with cloud optical depth (Platt et al. 1987).

In the analysis of cloud backscatter and extinction, the effects of backscatter and attenuation due to molecules and aerosols within the cloud must first be allowed for and removed. Such methods have been described recently by Platt et al. (1998). Now, (2) can also be written

$$\gamma'(\pi) = \frac{k}{2\overline{\eta}}(1 - \tau^2_{\text{eff}}), \tag{3}$$

where τ^2_{eff} is an effective two-way transmittance that includes the multiple-scattering factor $\eta(z_t, z_b)$. The symbol τ is frequently used to denote optical depth. However, the Radiation Commission of the International Association of Meteorology and Atmospheric Physics (IAMAP 1978) recommended τ as the symbol for transmittance and δ for optical depth, and, therefore, these are the notations used in this paper as well as earlier papers in the same series (e.g., Platt et al. 1987, 1998).

In the case of fully attenuating clouds τ^2_{eff} is zero, and from (3)

$$\gamma'(\pi) = \frac{k}{2\overline{\eta}} \quad \text{and therefore} \quad k = 2\overline{\eta}\gamma'(\pi). \tag{4}$$

In order to retrieve values of k, it is clear that the factor $\overline{\eta}$ must first be estimated. It also is noted that $k/(2\overline{\eta})$ can be retrieved from (3) in the case of a semitransparent cloud if the term τ^2_{eff} is measured.

b. Two-way transmittance τ^2_{eff}

The two-way transmittance can be estimated from a measurement of the scattering ratio R just above and below the cloud-top and cloud-base boundaries, respectively (e.g., Young 1995). The value $R(r)$ at range r is defined by

$$R(r) = \frac{B_c(r) + B_a(r) + B_m(r)}{B_m(r)}, \tag{5}$$

where the terms in the numerator represent the backscatter coefficients (m^{-1}) of cloud particles, aerosols, and molecules, respectively, and the denominator again represents molecular scattering. For a purely molecular atmosphere the scattering ratio is then equal to unity.

If $R(t)$ and $R(b)$ are the respective scattering ratios above cloud top and below cloud base, respectively, then we have the equations

$$R(t) = \frac{B_a(t) + B_m(t)}{B_m(t)}, \tag{6}$$

and

$$R(b) = \frac{[B_a(b) + B_m(b)]\tau_{\text{eff}}^2}{B_m(b)}. \tag{7}$$

Dividing (7) by (6) we obtain

$$\frac{R(b)}{R(t)} = \frac{B_m(t)[B_a(b) + B_m(b)]\tau_{\text{eff}}^2}{B_m(b)[B_a(t) + B_m(t)]}. \tag{8}$$

If we first assume that aerosol scattering is much less than molecular scattering, then

$$B_a(t) \ll B_m(t) \quad \text{and} \quad B_a(b) \ll B_m(b), \tag{9}$$

so that

$$\frac{R(b)}{R(t)} = \tau_{\text{eff}}^2. \tag{10}$$

The assumption of negligible aerosol backscatter clearly is not always justified, particularly as the Mount Pinatubo layer was still quite strong at the time of the LITE flight. However, an adjustment in τ_{eff}^2 can be made from a lidar backscatter profile when no cirrus is present. This adjustment depends on there being a break in the clouds close to the experimental area so that aerosol properties can be assumed to be the same (see section 5c). Also, if the 355-nm channel is employed, molecular scattering tends to be more dominant over aerosol scattering. It should be noted that τ_{eff}^2 is calculated here using the molecular backscatter outside the cloud boundaries. The multiple scattering through the cloud and, thus, the value of $\overline{\eta}$ will then be modified (e.g., Flesia and Starkov 1996). This might change the *dependence* of $\gamma'(\pi)$ on $1 - \tau_{\text{eff}}^2$ in (3), but will not change the deduced value of $k/(2\overline{\eta})$ when τ_{eff}^2 tends to zero because the lidar pulse does not then penetrate to cloud base.

c. Calculation of effective multiple-scattering factor

As mentioned earlier, in order to estimate values of k, the factor $\overline{\eta}$ must be estimated. Following Platt (1981), when the cloud is optically thick and the lidar pulse is fully occulted at some height above cloud base, then

$$\gamma'(\pi)_\infty(\text{TS}) = k/(2\overline{\eta}), \tag{11}$$

where $\gamma'(\pi)_\infty(\text{TS})$ is the total integrated scattering probability summed from cloud top to apparent cloud base. Similarly,

$$\gamma'(\pi)_\infty(\text{SS}) = k/2, \tag{12}$$

where $\gamma'(\pi)_\infty(\text{SS})$ is the total integrated single-scattering probability summed from cloud top to apparent base. Therefore,

$$\overline{\eta} = \frac{\gamma'(\pi)_\infty(\text{SS})}{\gamma'(\pi)_\infty(\text{TS})}. \tag{13}$$

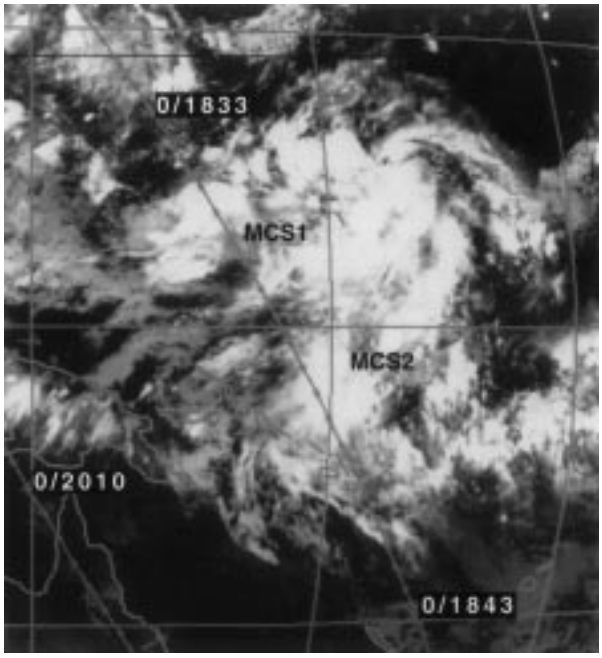

FIG. 1. A GMS image of the large cloud system containing MCS1 and MCS2, taken 10 Sep 1994. Orbit 13 and Mission Elapsed Time (MET) are superimposed. The image was taken at 1625 UTC, equivalent to an MET of 1802. The positions of MCS1 and MCS2 are labeled. The latitude line across the center of the image is the equator.

The probabilities normally are summed during a multiple-scattering calculation, and therefore $\overline{\eta}$ can be obtained easily. The detailed and well-established theoretical techniques outlined above are now applied to the various case studies described below.

4. Cloud systems

Apart from the isolated cirrus, the cloud systems all appeared to be MCSs, based on satellite images, and are designated as such.

a. Intense, active mesoscale convective system: MCS1

The area of convection considered here is shown just above the MCS1 label in the Geostationary Meteorological Satellite (GMS) infrared image of Fig. 1, taken at 1625 UTC 10 September 1994. The latitude and longitude ranges of the system are shown in Table 2. The convection represents part of a much larger system that appears to be in the process of becoming organized into a tropical storm. LITE passed approximately over the center of MCS1 and the corresponding image of backscatter intensity versus height and distance is shown in Fig. 2. The shuttle took about 50 s to cross the system, representing a distance of 350 km. The shuttle footprint crossed the center of MCS1 32 min after the GMS image was recorded. Along the orbit to the north and south of the MCS the clouds represent comparatively calmer

FIG. 2. LITE position–height image of MCS1 at 532-nm wavelength, together with regions to the north and south of MCS1. Lat = N, long = E, GMT = UTC h:min:s on 10 Sep 1994. The key gives the relative backscatter intensity (arbitrary).

conditions, although a cirrus shield is still present. There is also much midlevel cloud and towering cumulus. An enlarged image of the MCS1 system is shown in Fig. 3. This image also shows delineation of cloud boundaries using a technique described by Winker and Vaughan (1994), suitably modified to accommodate a downward-looking space lidar. The central parts of the disturbance are seen to reach to an altitude of over 17 km, which, according to National Meteorological Center forecast data, is above the tropopause height of 16.6 km. The image in Fig. 2 indicates that over the most intense part of the system there is no lidar backscatter showing above the system noise from below the cloud or from ground reflectance. The signal-to-noise ratio of the cloud backscatter was high, and any residual backscatter below cloud base would thus be very small. The cloud was thus assumed to be fully occulting.

b. Mature cirrus in aging mesoscale convective system: MCS2

The MCS2 is shown just to the southwest of its label in the GMS satellite image of Fig. 1. Its latitude and longitude ranges are given in Table 2. The time that the shuttle took to traverse this system was greater than 100 s, representing a horizontal distance of over 700 km. The shuttle footprint crossed the center of the LITE image of MCS2 37 min after the GMS image was recorded. The LITE image is shown in Fig. 4. MCS2 has a much more diffuse appearance than MCS1. The maximum apparent depth was about 7 km, indicating smaller extinction coefficients compared to those of MCS1. A careful assessment of τ_{eff}^2 indicated that molecular backscatter could just barely be detected below cloud base over much of the cloud, indicating that the cloud base was being reached in those regions. Although not shown in Fig. 4, some small fragments of cloud at about 1-km altitude were visible in a similar image at around 1838:10 Mission Elapsed Time (MET) 10 September 1994, verifying that there was penetration of the cloud at that time. The cloud top was also lower than for MCS1, varying between about 14 and 15 km in altitude. This lower cloud top again indicated a less vigorous system than MCS1. The MET is about 1 h 37 min ahead of UTC.

The original convection that probably formed the system was dissipating, leaving a deep extended cirrostratus shield (e.g., Webster and Stephens 1980). However, in some regions, there was evidence of fresh convective cumulus cloud tops penetrating the ''base'' of MCS2. Their positions are indicated by the arrows in Fig. 4. The backscatter coefficients above effective cloud base appeared to have the greatest values in these regions, with the extinction coefficients being correspondingly higher.

c. Isolated cirrus cloud

A patch of isolated cirrus cloud overlying some middle and lower layers was also investigated. The cirrus was situated in a more stable region between MCS1 and MCS2, and is described later in section 5c.

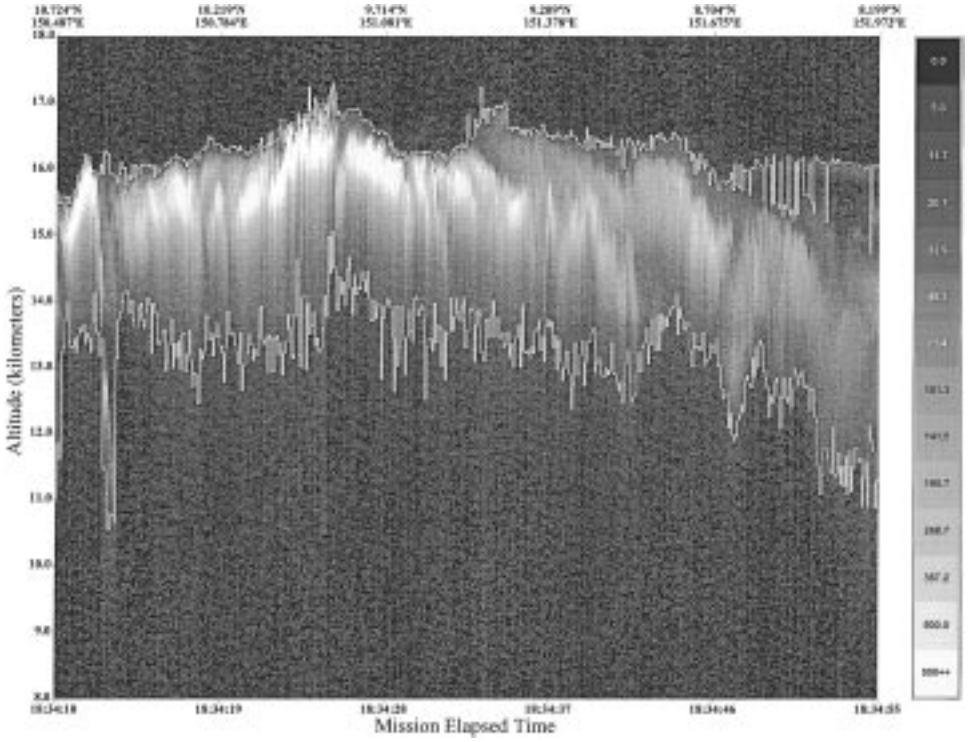

FIG. 3. Enlarged LITE image of MCS1, showing also the retrieved cloud boundaries in white, for 10 Sep 1994. Corresponding integrated backscatter values are given later in Fig. 10. The MET = h:min:s. The key gives the backscatter intensity in raw output counts.

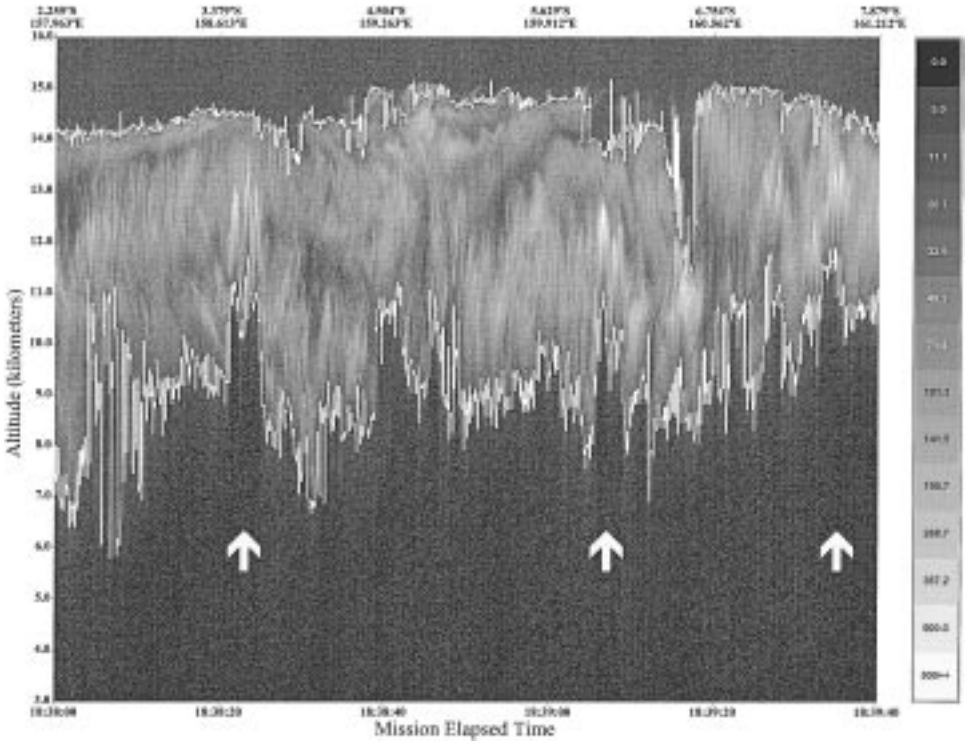

FIG. 4. LITE position–height image of MCS2 at 532-nm wavelength, showing also the retrieved cloud boundaries, for 10 Sep 1994. The arrows indicate the regions where fresh cumulus convection is occurring from below the cloud. Corresponding integrated backscatter values are given later in Fig. 12.

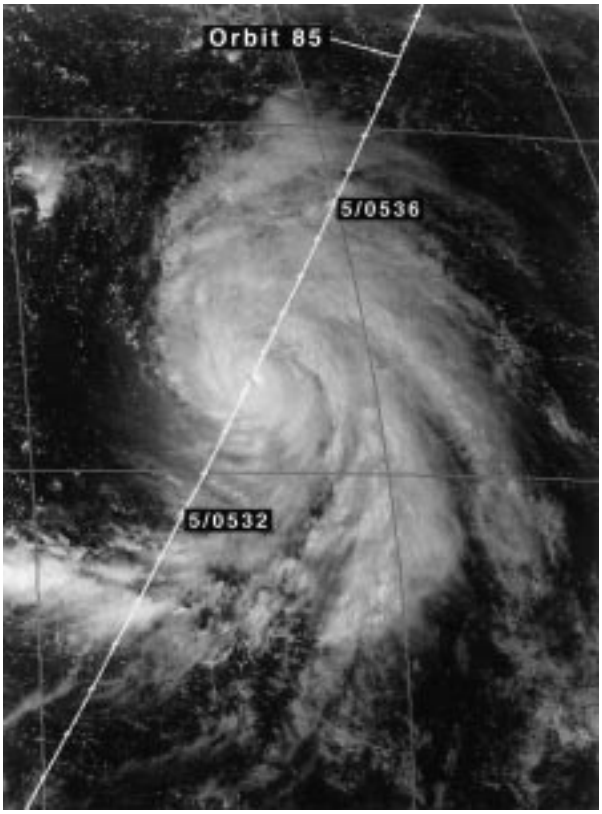

FIG. 5. GMS image showing Typhoon Melissa, with ascending orbit 85 superimposed, together with METs. The image was taken at 0425 UTC, equivalent to an MET of 0602, on 15 Sep 1994.

d. Cirrus capping active Typhoon Melissa: MCS3

The top cirrus layers of Typhoon Melissa were also investigated as a further case of vigorous convection. Although a typhoon is not considered always to be a mesoscale convective system, Melissa is here designated as MCS3. At the time of the MCS3 observations, Melissa was classed as a supertyphoon in its active phase, situated to the east of the Philippines. A supertyphoon experiences winds of 240 km h^{-1} or more near its center. These wind speeds make it roughly equivalent to a Class 5 hurricane on the Saffir–Simpson scale (e.g., Schneider 1996). A GMS image of the typhoon with LITE orbit 85 superimposed, taken at 0425 UTC 15 September 1994, is shown in Fig. 5. The distance–height representation obtained from LITE observations is shown in Fig. 6. The image covers a distance along the shuttle orbit footprint of about 1200 km. The footprint crossed the center of the LITE image of MCS3 28 min before the GMS image was recorded. The cloud appears to be completely occulting except over the eye where there is a clear region down to some stratus cloud near the surface. Any residual backscatter from low- or midlevel clouds was found from investigation of individual backscatter profiles to be below the background noise level and no surface reflection signal was apparent. The pulse penetration depth increases away from the eye, indicating a reduction in extinction coefficient. As in MCS2, there may have been some small pulse penetration below cloud base in some regions. For one thing, the daytime background noise level in MCS3 is higher than in the former two cases. There is also a sudden drop in cloud-top height from about 18 to 15.8 km some 140 km north of the eye. At the same point, the apparent pulse penetration changes from about 2 to 4 km. As in MCS1, the cloud top near the typhoon center was above the local NMC tropopause at 16.3 km.

e. Typhoon Melissa outflow area, indicating less convective cirrus clouds: MCS4

MCS4 was observed on 17 September 1994, two days after MCS3. The typhoon appeared to be in the decaying phase, and was located farther north compared to MCS3. The shuttle orbit crossed cloud bands situated away from the eye of the typhoon. The LITE image is shown in Fig. 7. The cloud is semitransparent for over half of the time, as indicated by the signals reflected from the surface and from midlevel and low cumulus clouds below the cirrus cloud base (cf. Typhoon Melissa in section 4d). The cloud depth penetrated is considerable. When the cloud was semitransparent (at, say, 0521:50 MET), the maximum (true) depth was as great as 7 km. The apparent decrease of cloud-base altitude due to pulse stretching from multiple scattering is considered to be minimal for cirrus clouds. The cloud-top altitude is seen to decrease toward the north from about 17 km down to 14.5 km. After about 0521 MET, the cloud bears a likeness to MCS2 in terms of its depth and transparency.

5. Analysis of systems in terms of integrated attenuated backscatter and transmittance

A preliminary analysis was first made on the real-time, 100-shot average, quicklook data and revealed dramatic changes in integrated attenuated backscatter across some of the convectively vigorous systems. A second detailed analysis using both 10-shot and single-shot profile averages from the high-rate dataset then was made and is described here. Wavelengths at 532 and 355 nm were used and their results were compared. The 355-nm data were found to be useful in terms of the strong molecular backscatter available. The lidar backscatter first was calibrated over a region in the upper troposphere where the measured backscatter profile fitted the calculated molecular profile, thus generating an ''attenuated system constant.'' This calibration allowed for attenuation between the chosen height and the top of the atmosphere, which would be nearly the same for both the cloud and the calibration height. Allowance was also made for differences in molecular attenuation between the calibration height and the cloud. Examples of data are shown in Figs. 8 and 9. A cloudless profile

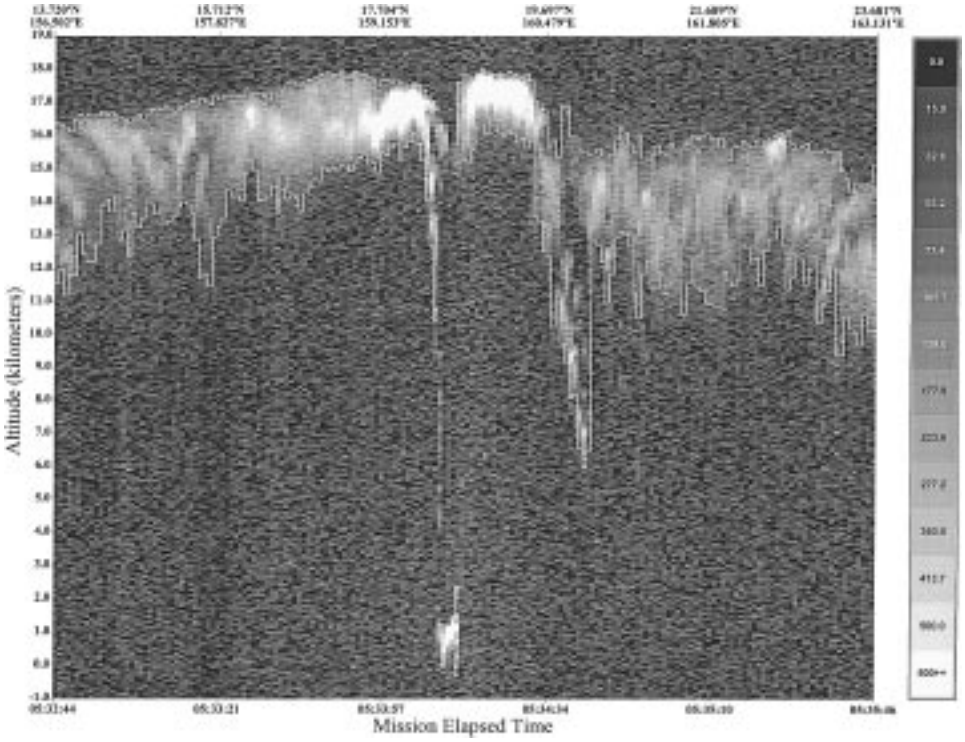

FIG. 6. LITE position–height image of Typhoon Melissa, MCS3, at 532 nm, showing the transit of the typhoon eye. Retrieved cloud image boundaries are also shown. Corresponding integrated backscatter values are given later in Fig. 15. METs are on 15 Sep 1994.

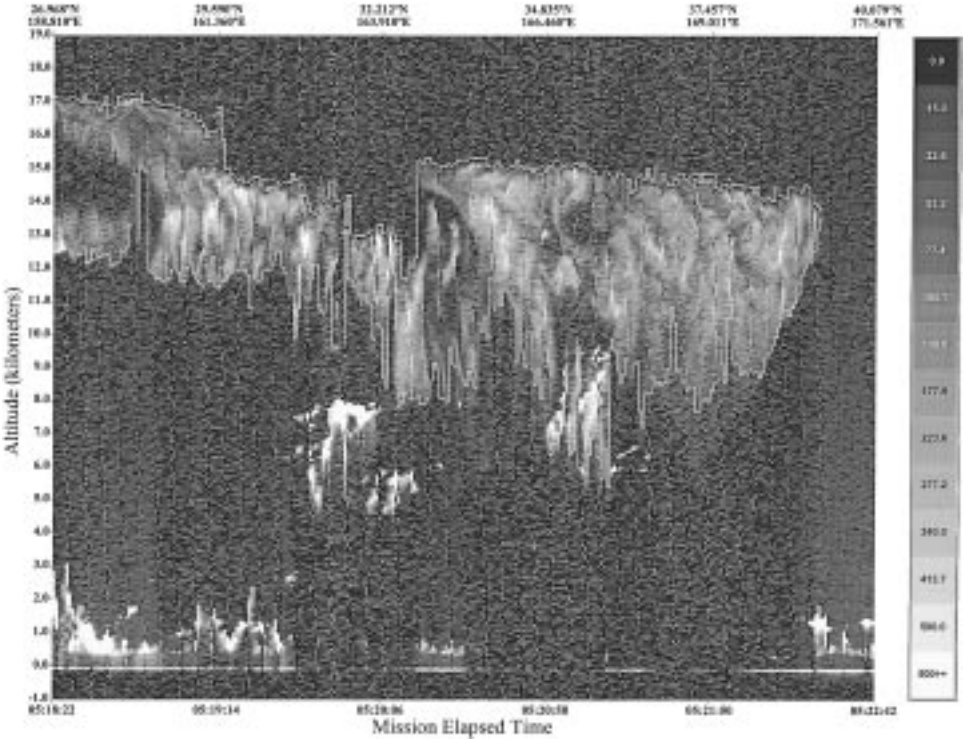

FIG. 7. LITE position–height image of Typhoon Melissa outer bands, MCS4, at 532 nm. The retrieved upper-cloud boundaries are also shown. Corresponding integrated backscatter values are given later in Fig. 16. METs are on 17 Sep 1994.

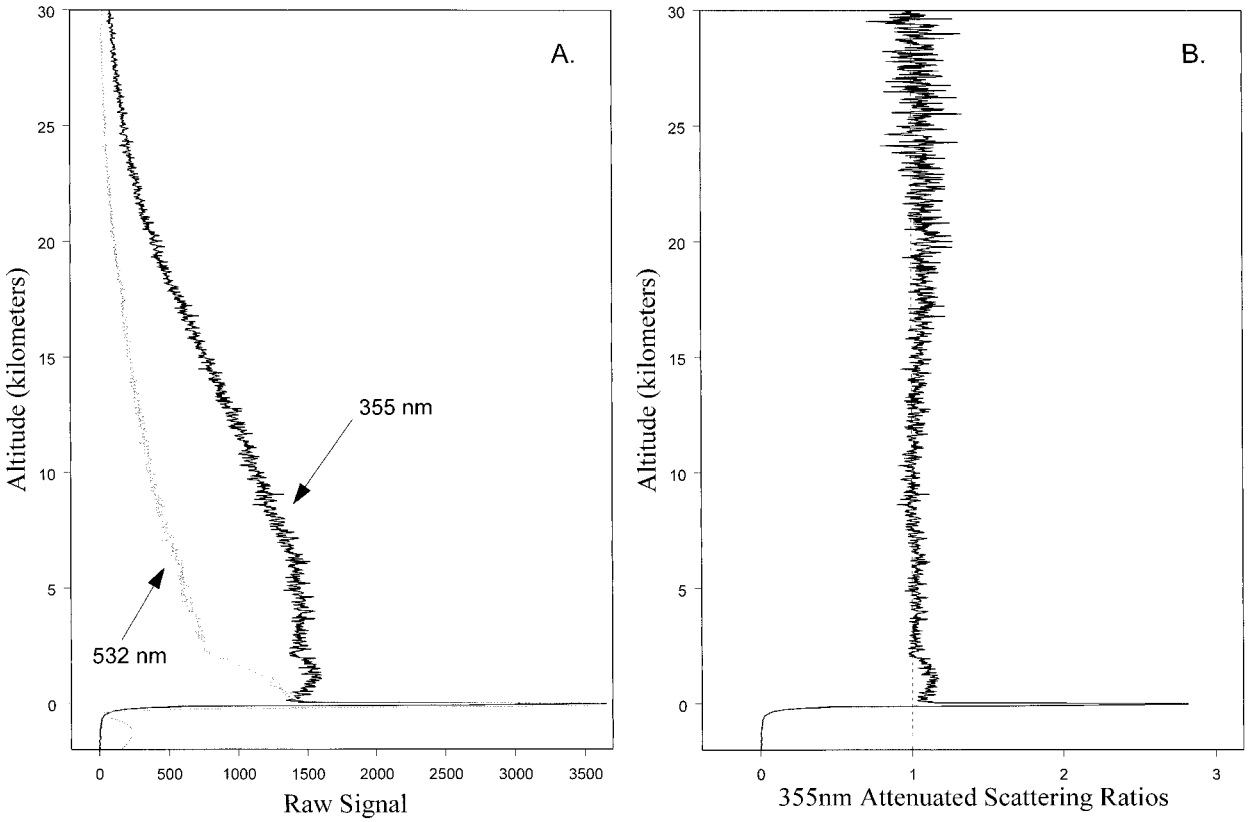

FIG. 8. (a) Single profiles of raw signal counts for a cloudless case at wavelengths of 355 and 532 nm. MET:2001:30–2001:40 12 Sep 1994. Latitude at end of integrating time: 19.38°S. (b) Same as (a), showing calculated scattering ratio at 355 nm.

that indicates the quality and attainable signal-to-noise ratio is shown in Figs. 8a and 8b. Figure 8b shows a fit of the 355-nm data to a molecular profile to provide a calibration. Figure 9a indicates the scattering ratio for one profile containing isolated cirrus, as constructed from the raw backscatter data in Fig. 9b.

Cloud boundaries were determined by the methods of Winker and Vaughan (1994). The effects of molecular backscatter within the cloud were removed by standard methods (e.g., Platt et al. 1998), and the calibrated cloud-attenuated backscatter then was integrated through the cloud depth.

a. Convectively active system: MCS1

Plots of $\gamma'(\pi)$ across MCS1 for both single-shot and 10-shot averages are shown in Fig. 10. The cloud was optically thick, as no molecular backscatter could be observed below effective cloud base above the background noise level, nor was there any measurable surface reflection. Thus, it was assumed that (4) was correct for the purposes of this analysis. Values of $\gamma'(\pi)$ fluctuate considerably with distance across the clouds with a fairly regular oscillation in the values and an envelope that defines maximum values. Values of $\gamma'(\pi)$ in this envelope vary from about 2.5 at 10.1°N down to 0.6 at 8.6°N. The single-shot values show a little more detail in the fluctuations than do the 10-shot values, indicating that some of the fluctuations had a scale of less than 7 km. The curves in Fig. 10 can be compared with the images in Figs. 2 and 3. The interesting point to be made here is that the variations in values of $\gamma'(\pi)$ *do not correspond* to variations in pulse penetration depth. Rather, variations in $\gamma'(\pi)$ are related to changes in the cloud backscatter phase function and appear to be *independent* of any changes in pulse penetration depth, which does not change much over the system and depends only on extinction coefficient. However, the largest values of $\gamma'(\pi)$ are close to the highest cloud tops attained. Figure 11 compares the integrated attenuated backscatter calculated for the 532- and 355-nm wavelengths. There is about a 16%–18% disparity between the two curves. This is due partly to uncertainties between the calibration constants in the two channels, which are estimated to be about 2% for the 355-nm channel and 6% for the 532-nm channel. Different molecular or aerosol attenuation in the 355-nm channel between the cloud and the top of the atmosphere was allowed for in the calibration. The additional disparity is attributed to different cloud backscatter coefficients at the two wavelengths. The differences are in any case systematic and both channels show the same large fluc-

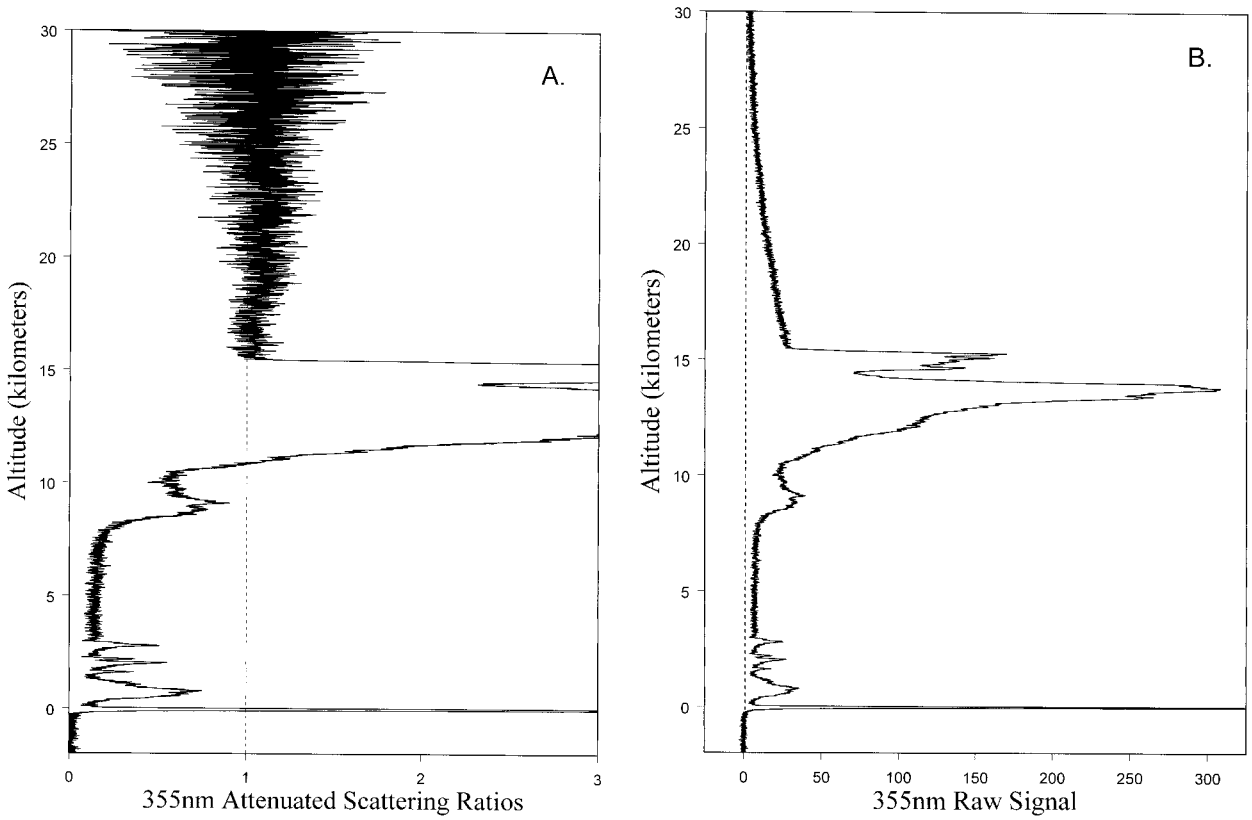

FIG. 9. (a) Calculated scattering ratio at 355 nm through a cirrus cloud. MET: 18:31:10–18:31:20 10 Sep 1994. Orbit 13, north of MCS1. (b) Backscatter coefficient at 355 nm of cloud in (a). Units are arbitrary.

tuations in $\gamma'(\pi)$. Values of $k/(2\overline{\eta})$ across MCS1 are considerably higher than any values retrieved from previous surface observations (Platt et al. 1998). The exceptions are values close to the edge of MCS1 beyond about 8.4°N latitude.

b. *Mature cirrus in MCS2*

Curves of $\gamma'(\pi)$ across MCS2 are shown in Fig. 12. Values vary between about 0.44 and 0.80. These values are much lower than those obtained at the center of MCS1, but are similar to those nearer the edges of that system. However, the lower values of $\gamma'(\pi)$ in MCS2

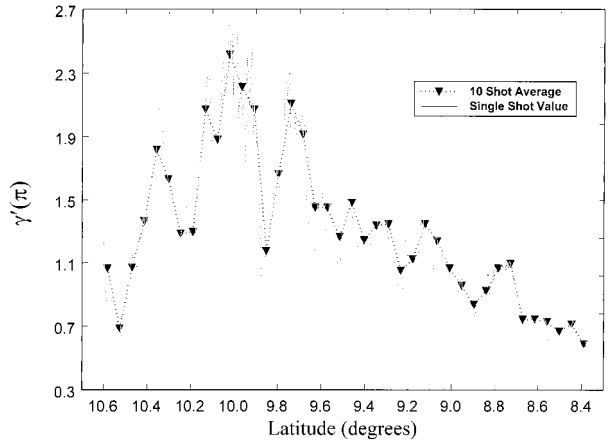

FIG. 10. Integrated attenuated backscatter $\gamma'(\pi)$ vs lat (N) for single- and 10-shot averages across MCS1 at a wavelength of 532 nm. Values refer to Fig. 2.

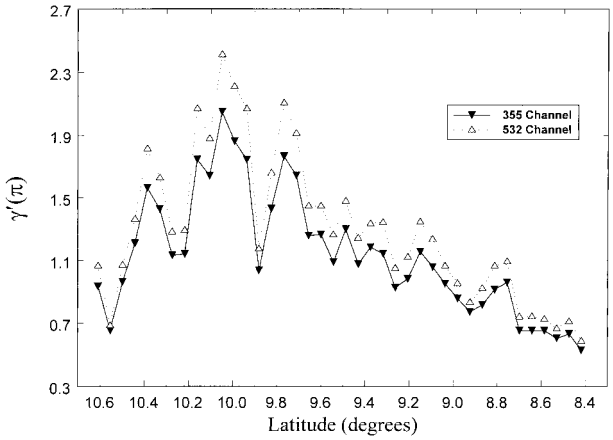

FIG. 11. Same as Fig. 10, but for wavelengths of 532 and 355 nm and 10-shot averages.

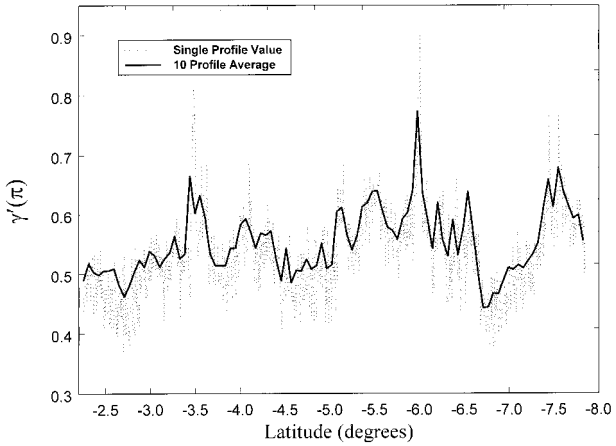

FIG. 12. Integrated attenuated backscatter $\gamma'(\pi)$ vs lat (S) across MCS2 for single- and 10-shot averages at 532 nm. Values refer to Fig. 4.

are generally *not* related to the greater cloud depth. For instance, similar values of $\gamma'(\pi)$ occur at 8.4°N latitude in MCS1 where the penetration depth is only about 2.5 km. As mentioned in section 4b, the cloud base in MCS2 was often just reached. However, there were several regions where the apparent cloud depth decreased, as indicated by the arrows in Fig. 4. In these regions, no molecular backscatter below cloud base could be detected and the highest backscatter coefficients were recorded. They were assumed to indicate the presence of fresh convective towers rising into the cirrus deck. There were indications that the value of $\gamma'(\pi)$ similarly increased in those regions. Values of $\gamma'(\pi)$ at 532 nm were again greater than at 355 nm by about 15%. For purposes of analysis, (4) still was considered to be a good approximation.

c. Isolated cirrus cloud

A region of isolated cirrus cloud between MCS1 and MCS2 also was analyzed. As shown in Fig. 13, it covered a region of about 420 km and was semitransparent over most of that region. Analyzed values of $1 - \tau_{\text{eff}}^2$ plotted against $\gamma'(\pi)$ are shown in Fig. 14. Only the top cirrus clouds that are delineated by the white boundaries were considered. The transmittance was determined using (6)–(10). The 355-nm channel was used in order to obtain sufficient molecular scattering below cloud base. Figure 14 shows a fairly linear dependence of $\gamma'(\pi)$ on $1 - \tau_{\text{eff}}^2$, as predicted by (3) for the case when the multiple-scattering factor is constant. Deviations in η, or possibly k, with optical depth would show up as deviations in the linearity between $\gamma'(\pi)$ and $1 - \tau_{\text{eff}}^2$. However, such deviations are not detectable within the scatter of the data, although values of $\gamma'(\pi)$ are slightly low for higher values of $1 - \tau_{\text{eff}}^2$. The average value of $k/(2\overline{\eta})$ (for $\tau_{\text{eff}}^2 = 0$) was 0.35.

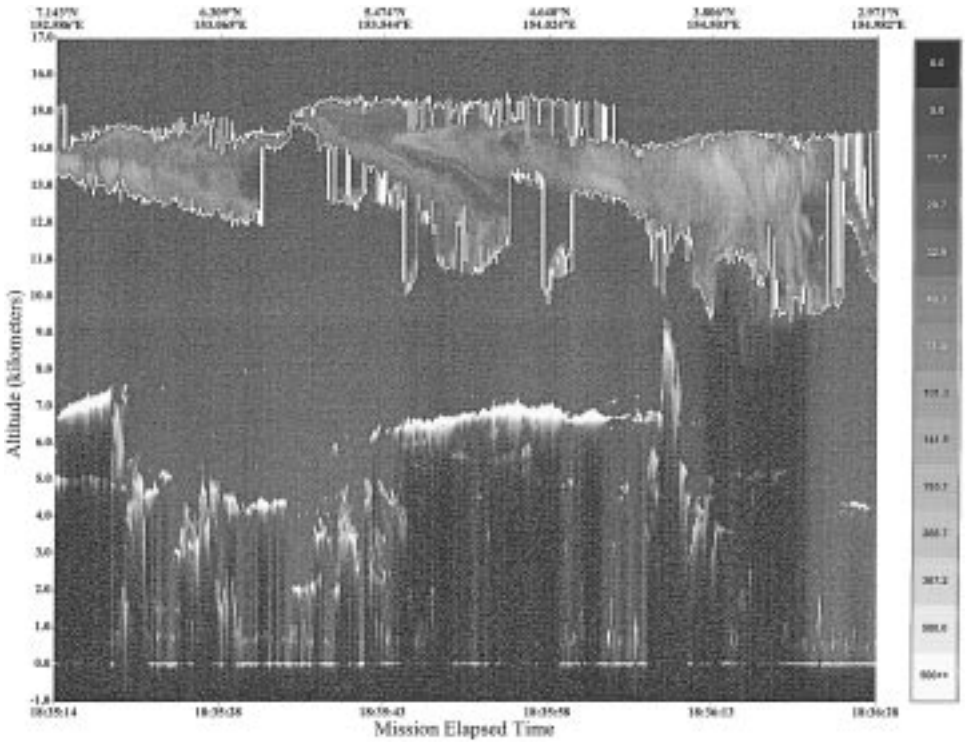

FIG. 13. LITE distance–height image of attenuated backscatter for a region between MCS1 and MCS2 for 10 Sep 1994. Retrieved cirrus cloud boundaries are also shown.

d. Vigorous convection in MCS3

A satellite image of Typhoon Melissa and a distance–height image of backscatter intensity are shown in Figs. 5 and 6, respectively. The lidar backscatter profiles were taken on a daytime ascending orbit and the solar photon background noise under these conditions was too strong to allow retrieval of cloud transmittance. However, the integrated backscatter still could be calculated once allowance was made for the different daytime gain and filter settings on the lidar. Single lidar shots were checked for signal saturation in the cloud. The direct current background signal due to the solar radiance had been subtracted for each profile during the mission so as to keep the backscatter on scale (Winker et al. 1996). Values of $\gamma'(\pi)$, that is, $k/(2\overline{\eta})$, were found to increase to a maximum of 1.64 near the eye of the typhoon, falling off to values between 0.5 and 1.0 (Fig. 15). The value 1.64 was again very high compared to surface-measured values at equivalent temperatures.

e. Decaying typhoon outflow: MCS4

The time–height image is shown in Fig. 7. The analyzed cirrus clouds are delineated by the white cloud boundaries. The variation in integrated backscatter across the system is shown in Fig. 16. It was not possible to obtain cloud transmittance in the regions of semitransparent cloud because of the high daytime noise level. However, there were two regions where the surface reflection was below the background noise, indicating occultation of the pulse. The values of $\gamma'(\pi)$ in those regions varied from about 0.38 to 0.65. These values were in the ranges found in the isolated cirrus, in MCS2, and near the edges of MCS1 and MCS3.

6. Discussion

a. Measured values of $k/(2\overline{\eta})$

The values of the cloud particle effective backscatter-to-extinction ratio $k/(2\overline{\eta})$ found for cirrus ice clouds in this study showed considerable variations. The results are summarized in Table 3, in terms of cloud temperature. The coldest clouds near the tropopause, as exemplified by MCS1 and MCS3, correspond to the most energetic convective areas: a large mesoscale system and a typhoon, respectively. In these cases, values of $k/(2\overline{\eta})$ reach maximum values that are five to eight times greater than the values found at lower temperatures, but with lower values near the observed edges of MCS1 and MCS3. It also is apparent that even the lower values found in LITE are generally greater than the tropical cirrus values found from ground-based sensing at equivalent temperatures (Platt et al. 1998), which also are shown in Table 3. The differences could be due partially to the different types of cirrus studied, but the isolated cirrus in this study also exhibited a higher value. The differences also can be attributed to smaller multiple-scattering factors at space ranges, as discussed below.

b. Calculated values of k, $\overline{\eta}$, and $k/(2\overline{\eta})$

As a comparison with the LITE results, values of k, $\overline{\eta}$, and $k/(2\overline{\eta})$ for space-based soundings were calculated (Table 4). The calculations by Platt were based on Platt (1981) code and phase functions. They were made prior to this study but have not been published elsewhere. Values given by Winker were calculated for this study using the code described in Winker and Poole (1995) and the scattering phase functions of Yang and Liou (1996). Values under Miller used a code from Miller and Stephens (1999) and the phase functions of Takano and Liou (1995). The latter authors and Yang and Liou (1996) both used sophisticated ray-tracing (matrix) methods to generate their scattering phase functions, but the phase functions used by Platt (1981) were generated from both theoretical and empirical data.

Theoretical values of k in Table 4 appear to be highest for solid hexagonal columns and plates. However, values for columns vary between 1.628 and 0.708 so that the various theoretical codes give somewhat disparate results. Macke and Mischenko (1996) obtained an intermediate value of 1.05. Dendrites and capped columns also exhibit high values of k and bullet rosettes give a lower value.

Generally, it is found that experimental values tend to be lower than the above examples of regular ''perfect'' crystals. Platt (1981) used a range of values of k in his calculations. The values varied from 0.016 to 0.205, and were based on empirical and some theoretical values from that time. Sassen (1978) determined values of k equal to 0.26 for spatial crystals and 0.41 for more complex crystals. Sassen and Liou (1979) determined values between 0.1 and 0.2 for a mix of plate and hexagonal crystals. Both of the above were laboratory experiments. These values of k are also very similar to the range of values retrieved from lidar-integrated backscatter in the PROBE and shown in Table 3.

In an attempt to reduce values of the asymmetry parameter of cirrus clouds that were too high compared to observation, various imperfections were introduced into perfect-crystal models of scattering. For example, Macke and Mischenko (1996) used a method of distortion of a hexagonal crystal to lower the calculated asymmetry parameter. Coincidentally, the prescribed distortion for an optimum asymmetry parameter also led to a value of k of about 0.18. Macke and Mischenko (1996) concluded that ''scattering at regular particles is not always representative of real atmospheric particles''. The ground-based lidar observations of k are consistent with this statement. Hess et al. (1998) also used a model of distorted regular hexagons and came to the same conclusions, with values of k again in the region of 0.15–0.3 as deduced from their published scattering phase functions.

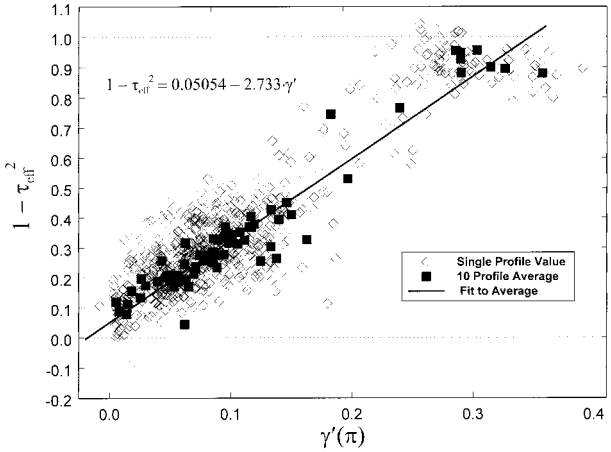

FIG. 14. Plot of $1 - \tau_{\text{eff}}^2$ vs $\gamma'(\pi)$ at 355 nm for the region shown in Fig. 13. Single profile and 10-profile averages are shown.

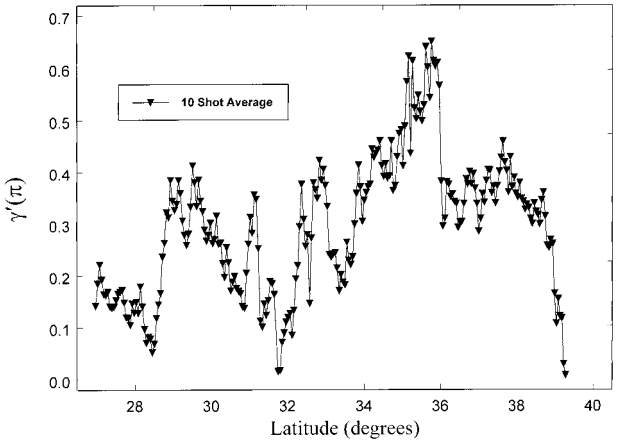

FIG. 16. Plot of integrated attenuated backscatter $\gamma'(\pi)$ vs lat (N) across MCS4: 10-shot averages at 532 nm. Values refer to Fig. 7.

The measured LITE values considered here, are for the quantity $k/(2\overline{\eta})$ rather than k, and values of $\overline{\eta}$ are not well known for space ranges. Values of $\overline{\eta}$ that have been calculated for this study are shown in Table 4. There are certain characteristics of $\overline{\eta}$ that must be considered. First, $\overline{\eta}$ is correlated with k. This correlation is because the single scattering is determined by the value of k, whereas multiple scattering is determined by scattering intensities away from the back direction. Platt (1981) demonstrated this aspect of lidar sounding by creating three phase functions (series 1–3 in Table 4) with similar angular scattering properties except near to the back direction. The increase in $\overline{\eta}$ with k for space ranges in Table 4 is very evident in the Platt values.

Second, space values of $\overline{\eta}$ will tend to be less than ground-based values because of the well-known range effect (Platt 1981; Spinhirne 1982). Now, the ground-based values of $\overline{\eta}$ in Table 3 were generated also from series-3 data for different cloud ranges (temperatures). It is apparent from Tables 3 and 4 that the series-3 space value of $\overline{\eta}$ is about a factor of 2 smaller than the average ground-based value. (Note that Winker, using the Platt series-3 phase function but a different Monte Carlo code obtained a slightly higher value for $\overline{\eta}$). Some experimental evidence for the lower space values of $\overline{\eta}$ compared to those observed from ground-based ranges is given by Pelon et al. (1996) from the European LITE Correlative Measurements Campaign. They were able to observe a cirrus cloud with lidar from an aircraft that flew above the cirrus and along the LITE orbit simultaneously with LITE. Some of their results, reproduced by Winker (1997), suggest that the value of $\overline{\eta}$ from space was about 2.5 times smaller than the value observed from the aircraft. More evidence is obtained from Spinhirne et al. (1982), who measured from aircraft lidar a penetration depth of only 0.3 km in a thunderstorm top at 14 km. This depth is much less than those measured in MCS1 and MCS3, again indicating (assuming similar extinctions) a much lower multiple-scattering factor in the latter cases. A considerable discrepancy also exists between the two values of $\overline{\eta}$ for hollow columns in Table 4. The calculations of Miller give a very small value (0.027) compared to that calculated by Winker (0.25). Miller took the calculations to a much higher cloud optical depth than did Winker, which might have some

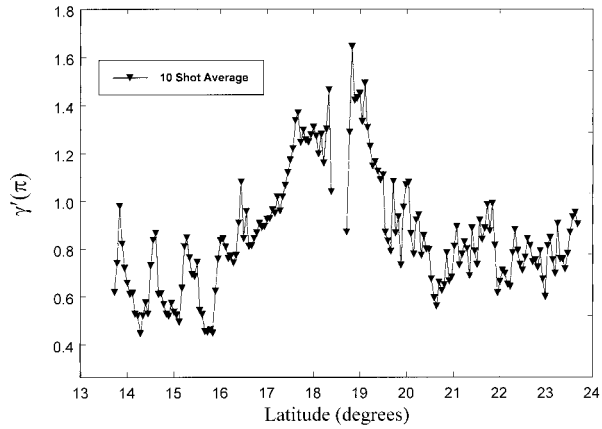

FIG. 15. Plot of integrated attenuated backscatter $\gamma'(\pi)$ vs lat (N) across Typhoon Melissa: 10-shot averages at 532 nm. Values refer to Fig. 6.

TABLE 3. Values of effective backscatter-to-extinction ratio of cirrus measured in the LITE project compared to ground-based values measured in the Pilot Radiation Observation Experiment (PROBE; Platt et al. 1998).

Temperature range (°C)	LITE cirrus in this study, range of $k/(2\overline{\eta})$	PROBE cirrus, mean $k/(2\overline{\eta})$	PROBE cirrus, estimated $\overline{\eta}$	PROBE cirrus, calculated k
−75 to −65	0.3–2.5	0.14	0.30	0.08
−65 to −55	0.36–0.5	0.18	0.36	0.13
−55 to −45	0.5–0.8	0.22	0.42	0.18
−45 to −35	0.35–0.45	0.29	0.48	0.28

TABLE 4. Calculated values of effective multiple-scattering factor $\overline{\eta}$ from space. The figures in parentheses in the headings of column 1 represent telescope field of view, range to cloud, and cloud optical depth, respectively.

	k	$\overline{\eta}$	$k/(2\overline{\eta})$
Platt (3.5 mrad, 200 km, $\delta = 8$)[a]			
Series 1[d]	0.016	0.077 (0.099)	0.104 (0.081)
Series 2[d]	0.108	0.175 (0.199)	0.309 (0.271)
Series 3[d]	0.205	0.203 (0.224)	0.504 (0.453)
Winker (3.5 mrad, 293 km, $\delta = 10$)[b]			
Hexagonal column (200 μm/40 μm)	1.607	0.41	1.95
Hexagonal column (50 μm/10 μm)	1.628	0.50	1.63
Hollow hexagonal column	0.077	0.25	0.15
Hexagonal plate	1.278	0.34	1.87
Platt Series 3	0.216	0.24	0.46
Cirrus—Takano and Liou (1989)	1.204	0.54	1.11
Miller (3.5 mrad, 293 km, $\delta = 21$)[c]			
Dendrite	0.928	0.298	1.56
Capped column	0.923	0.291	1.59
Bullet rosette	0.574	0.180	1.59
Hollow column	0.060	0.027	1.11
Solid column	0.708	0.239	1.48

[a] Calculated by method of Platt (1981) from empirical phase functions used in the same paper.
[b] Calculated by method of Winker and Poole (1995) from the data of Yang and Liou (1996), except where shown.
[c] Calculated by method of Miller and Stephens (1999) from the data of Takano and Liou (1995).
[d] Values in parentheses are for a daytime LITE telescope aperture of 1.1 mrad.

bearing on the difference. Platt, however, was able to extrapolate his values of $\overline{\eta}$ to higher optical depths.

We can now attempt to link the theoretical values of $k/(2\overline{\eta})$ in Table 4 with the observed LITE values. Observed values in column 2 of Table 3 that occur between cloud temperatures of $-65°$ and $-35°$C vary mainly between 0.36 and 0.5 but with occasional values as high as 0.8. These values agree approximately with those obtained from Platt's series 2 and 3. Pelon et al. (1996) also retrieved values of $k/(2\overline{\eta})$ of about 0.45–0.50 in LITE data observed over northern Europe. Taking into account the higher values of $\overline{\eta}$ in the ground-based case, the LITE values are also compatible with the PROBE lidar data. Thus, the LITE values in the above temperature range can be considered to be compatible with ground-based values. It follows that they also are consistent with laboratory measurements and with theoretical computations using models of distorted hexagonal crystals.

We now turn to the interpretation of the much higher values of $k/(2\overline{\eta})$ that were observed from LITE near the center of the strong systems MCS1 and MCS3. Typically, values between 0.7 and 2.5 were observed (Figs. 10 and 15) in these regions, although lower values more compatible with ''typical'' cirrus were observed near the edges of these systems. Based on Table 4, it is tempting to assign this high range of measured values of $k/(2\overline{\eta})$ to scattering from regular solid hexagonal columns, plates, dendrites, or capped columns. The emphasis here is on ''regular'' rather than distorted columns. Whether this assignment is valid near the tops of strong mesoscale systems is discussed in the next section.

There are also several reasons why the above assignment for the high LITE values is subject to considerable uncertainty. First, the ray-tracing and other methods used may not give very accurate values of scattering functions in the back direction, as exemplified by the wide differences in k found by Takano and Liou (1995), Yang and Liou (1996), and Macke and Mischenko (1996) for solid hexagonal columns. Second, it is known that calculated values of $\overline{\eta}$ for any given ''standard'' cloud are found to depend considerably on the approximations used in a given multiple-scattering model [e.g., Bissonnette et al. (1995)], leading to another source of uncertainty. Further, the apparent variation in calculated values of $\overline{\eta}$ with optical depth, even at high values of this quantity, has not been fully explored.

Third, it could be argued that the observed variations in $k/(2\overline{\eta})$ are due to variations in $\overline{\eta}$ rather than in k, caused by differences in particle size, that would affect the width of the diffraction peak of the phase function. Such an effect is illustrated in Table 4 by the two examples of hexagonal columns that had different dimensions but similar values of k (1.607 and 1.628). The value of $\overline{\eta}$ decreases by about 20% for the larger column. Thus, crystal size also has some effect on observed values of $k/(2\overline{\eta})$, although it seems unlikely that this could account for the total variations in $k/(2\overline{\eta})$. It is more likely that the variations were due partially to changes in k and, to a lesser extent, to changes in $\overline{\eta}$, that is, a mixture of changes in particle size and habit.

Now, in the case of the isolated cirrus shown in Figure 14, any variations in $\overline{\eta}$ would show up as deviations from the fitted curve. However, within the scatter of the

data, these deviations were not appreciable, thus putting a limit on any variations in $\overline{\eta}$.

c. Microphysics in tropical MCS cirrus

The values of $k/(2\overline{\eta})$ found in this study indicate that the cirrus microphysics near the centers of the strongly convective MCSs (MCS1 and MCS3) may be different compared with that in the more aging cirrus systems and in isolated cirrus. This difference is not surprising because the former cirrus layers were probably the result of strong convective updrafts as compared to the latter layers where updrafts were probably weak. What is perhaps surprising is the observed high values of $k/(2\overline{\eta})$, which might indicate, based on Table 4, the presence of regular pristine types of crystal of the solid hexagonal column or similar variety. One would expect, however, more irregular or indeterminate crystals in strong updrafts, as found in the in situ observations of McFarquhar and Heymsfield (1996) that were taken in tropical anvil outflows at temperatures between $-50°$ to $-40°$C. However, the top MCS1 and MCS3 layers were very cold, with temperatures near $-70°$C. The larger, more complex crystals might fall out quickly or never reach such altitudes, thus leaving smaller crystals that have experienced slower growth rates (e.g., Jensen et al. 1996). In support of this assumption, KN measured considerable numbers of small particles near the tops of tropical storms over northern Australia. They could not obtain the crystal habits, but particle radii were in the range of 1–50 μm with an effective radius of 7 μm. Such small crystals would have a simpler crystal structure. They would also give a larger visible extinction coefficient for a given ice content. The largest cloud extinction coefficients (smallest pulse penetration depths) certainly occurred in the regions of the highest values of $k/(2\overline{\eta})$. Aircraft lidar observations by Spinhirne et al. (1983) over the tops of strong thunderstorms indicated a layer with high backscatter, strong extinction, and a depolarization ratio from 0.4 to 0.7. These observations led to the conclusion that the layers were ice and contained a great many (small) particles in the strong updrafts. These findings would then agree qualitatively with the LITE observations. However, the presence of small crystals would indicate wider diffraction peaks and thus higher values of $\overline{\eta}$, which would not be consistent with the higher values of $k/(2\overline{\eta})$. Thus the high values of $k/(2\overline{\eta})$ were more likely caused by high values of k.

7. Summary and conclusions

Significant variations in integrated attenuated backscatter have been found to occur in occulting cirrus layers at the tops of some large tropical MCSs and in attenuating regions of isolated cirrus. Much of the cirrus with temperature ranges between $-35°$ and $-65°$C had values of $k/(2\overline{\eta})$ that were within the ranges of computed values for scattering functions based on ''imperfect'' distorted hexagonal crystals. Such cirrus also had values that were within the range of laboratory values and measured ground-based values, when differences in the values of $\overline{\eta}$ between satellite and ground-based lidar are allowed for.

At the lowest temperature range, between $-65°$ and $-75°$C, some of the values of $k/(2\overline{\eta})$ (near the centers of MCS1 and MCS3) were quite different, indicating that the very cold cirrus in the strong convective regions had different properties compared with the other cirrus layers. From theoretical calculations of crystal scattering functions together with calculations of the multiple-scattering effects, the high values of $k/(2\overline{\eta})$ were found to be consistent with a model of well-formed regular hexagonal columns or plates that probably have small dimensions. However, because of the uncertainties in the values of k and $\overline{\eta}$ that arise from imperfect knowledge of cirrus crystals and their scattering functions, the above interpretations of the high values of $k/(2\overline{\eta})$ must remain tentative for now. More extensive microphysical measurements in high tropical MCS clouds and other cirrus clouds are required to provide experimental validation. More extensive calculations on the multiple-scattering factor and its variation at high values of optical depth also are required.

The data demonstrate the power of a space lidar (or high-flying aircraft) to investigate in detail cirrus clouds at the tops of convectively active systems that cannot be observed from the ground. Such clouds have been shown to be important radiatively. Miller and Frank (1993) showed that radiative cooling at the tops of tropical cloud clusters increased predicted precipitation by 2 mm h^{-1} irrespective of which model they used. Tao et al. (1996) found that large-scale radiative cooling in the Tropics, which also increased significantly over cloud clusters, led to greater humidity and a 36% increase in rainfall in the Tropics. The presence of small crystals in the top radiating layers of the clouds would radically change the radiation balance of the clouds. Chen et al. (1996) defined disturbances such as those shown in Fig. 1 as cloud superclusters. The LITE data provide the first distance–height traverse across the top of such a supercluster.

Acknowledgments. The authors would like to thank the many people associated with the LITE project for their support during the experiment, particularly Dr. M. P. McCormick, together with other members of the Science Team. C. M. R. Platt was employed by the Science and Technology Corporation, Hampton, Virginia, for three months in 1995. C. M. R. Platt would like also to thank the Aerosol Branch of the NASA Langley Research Center for much support and encouragement.

REFERENCES

Bissonnette, L. R., and Coauthors, 1995: LIDAR multiple scattering from clouds. *Appl. Phys. B,* **60,** 355–362.

Chen, S. S., R. A. Houze Jr., and B. E. Mapes, 1996: Multiscale variability of deep convection in relation to large-scale circulation in TOGA COARE. *J. Atmos. Sci.,* **53,** 1380–1409.

Couch, R. H., and Coauthors, 1991: Lidar In-space Technology Experiment (LITE): NASA's first in-space lidar system for atmospheric research. *Opt. Eng.,* **30,** 88–95.

Flesia, C., and A. V. Starkov, 1996: Multiple scattering from clear atmosphere obscured by transparent crystal clouds in satellite-borne lidar sensing. *Appl. Opt.,* **35,** 2637–2641.

Hess, M., R. B. A. Koelemeijer, and P. Stammes, 1998: Scattering matrices of imperfect hexagonal ice crystals. *J. Quant. Spectrosc. Radiat. Transfer.,* **60,** 301–308.

Heymsfield, A. J., and G. M. McFarquhar, 1996: High albedos of cirrus in the Tropical Pacific Warm Pool: Microphysical interpretation from CEPEX and from Kwajalein, Marshall Islands. *J. Atmos. Sci.,* **53,** 2424–2451.

IAMAP, 1978: Terminology and units of radiation quantities and measurements. *International Association of Meteorology and Atmospheric Physics, Radiation Commission,* E. Raschke, Ed., IAMAP, 17 pp.

Jensen, E. J., O. B. Toon, H. B. Selkirk, J. D. Spinhirne, and M. R. Schoeberl, 1996: On the formation and persistence of subvisible cirrus clouds near the tropical tropopause. *J. Geophys. Res.,* **101,** 21 361–21 375.

Knollenberg, R. G., K. Kelly, and J. C. Wilson, 1993: Measurements of high number densities of ice crystals in the tops of tropical cumulonimbus. *J. Geophys. Res.,* **98,** 8639–8664.

Macke, A., and M. I. Mischenko, 1996: Applicability of regular particle shapes in light scattering calculations for atmospheric ice particles. *Appl. Opt.,* **35,** 4291–4296.

McCormick, M. P., and Coauthors, 1993: Scientific investigations planned for the Lidar In-Space Technology Experiment (LITE). *Bull. Amer. Meteor. Soc.,* **74,** 205–214.

McFarquhar, G. M., and A. J. Heymsfield, 1996: Microphysical characteristics of three anvils sampled during the Central Equatorial Pacific Experiment. *J. Atmos. Sci.,* **53,** 2401–2423.

Miller, R. M., and W. M. Frank, 1993: Radiative forcing of simulated tropical cloud clusters. *Mon. Wea. Rev.,* **121,** 482–498.

Miller, S. D., and G. L. Stephens, 1999: Multiple scattering effects in the lidar pulse stretching problem. *J. Geophys. Res.,* in press.

Pelon, J., F. Nicolas, and P. H. Flamant, 1996: On the multiple scattering contribution in backscattered lidar signals for spaceborne observations, *Proc. Int. Workshop on Spaceborne Lidar—Technology and Applications.* Hakone, Japan, National Space Development Agency of Japan, Earth Science and Technology Forum/Earth Science and Technology Organization, 423–430.

Platt, C. M. R., 1973: Lidar and radiometric observations of cirrus clouds. *J. Atmos. Sci.,* **30,** 1191–1204.

——, 1979: Remote sounding of high clouds. I: Calculation of visible and infrared optical properties from lidar and radiometer measurements. *J. Appl. Meteor.,* **18,** 1130–1143.

——, 1981: Remote sounding of high clouds. III: Monte Carlo calculations of multiple-scattered lidar returns. *J. Atmos. Sci.,* **38,** 156–167.

——, J. C. Scott, and A. C. Dilley, 1987: Remote sounding of high clouds. VI: Optical properties of midlatitude and tropical cirrus. *J. Atmos. Sci.,* **44,** 729–747.

——, S. A. Young, P. J. Manson, G. R. Patterson, S. C. Marsden, R. T. Austin, and J. Churnside, 1998: The optical properties of equatorial cirrus from observations in the ARM Pilot Radiation Observation Experiment. *J. Atmos. Sci.,* **55,** 1977–1996.

Sassen, K., 1978: Backscattering cross sections for hydrometeors: Measurements at 6328 Å. *Appl. Opt.,* **17,** 804–806.

——, and K. N. Liou, 1979: Scattering of polarized laser light by water droplet, mixed-phase and ice crystal clouds. Part I: Angular scattering patterns. *J. Atmos. Sci.,* **36,** 838–851.

Schneider, S. H., 1996: *Encyclopaedia of Climate and Weather.* Oxford University Press, 929 pp.

Spinhirne, J. D., 1982: Lidar clear atmosphere multiple scattering dependence on receiver range. *Appl. Opt.,* **21,** 2467–2468.

——, M. Z. Hansen, and L. O. Caudill, 1982: Cloud top remote sensing by airborne lidar. *Appl. Opt.,* **21,** 1564–1571.

——, ——, and J. Simpson, 1983: The structure and phase of cloud tops as observed by polarization lidar. *J. Climate Appl. Meteor.,* **22,** 1319–1331.

Takano, Y., and K. N. Liou, 1989: Solar radiative transfer in cirrus clouds. Part I: Single-scattering and optical properties of hexagonal ice crystals. *J. Atmos. Sci.,* **46,** 3–18.

——, and ——, 1995: Radiative transfer in cirrus clouds. Part III: Light scattering by irregular ice crystals. *J. Atmos. Sci.,* **52,** 818–837.

Tao, W.-K., S. Lang, J. Simpson, C.-H. Sui, B. Ferrier, and M.-D. Chou, 1996: Mechanisms of cloud–radiation interaction in the Tropics and midlatitudes. *J. Atmos. Sci.,* **53,** 2624–2651.

Webster, P. J. and G. L. Stephens, 1980: Tropical upper-tropospheric extended clouds: Inferences from Winter MONEX. *J. Atmos. Sci.,* **37,** 1521–1541.

Winker, D. M., 1997: Simulation and modeling of multiple scattering effects observed in LITE data. *Advances in Atmospheric Remote Sensing by Lidar, Selected Papers of the International Laser Radar Conference (ILRC),* A. Ansmann et al., Eds., 185–188.

——, and M. A. Vaughan, 1994: Vertical distribution of clouds over Hampton, Virginia, observed by lidar under the ECLIPS and FIRE ETO programs. *Atmos. Res.,* **34,** 117–133.

——, and L. R. Poole, 1995: Monte-Carlo calculations of cloud returns for ground-based and space-based lidars. *Appl. Phys. B,* **60,** 341–344.

——, R. H. Couch, and P. M. McCormick, 1996: An overview of LITE: NASA's Lidar In-space Technology Experiment. *Proc. IEEE.,* **84,** 1–17.

Wong, T., G. L. Stephens, P. W. Stackhouse Jr., and F. P. J. Valero, 1993: The radiative budgets of a tropical mesoscale convective system during the EMEX-STEP-AMEX experiment. 1: Observations. *J. Geophys. Res.,* **98,** 8683–8693.

Yang, P., and K. N. Liou, 1996: Geometric-optics-integral-equation method for light scattering by non-spherical ice crystals. *Appl. Opt.,* **35,** 6568–6584.

Young, S. A., 1995: Analysis of lidar backscatter profiles in optically thin clouds. *Appl. Opt.,* **34,** 7019–7031.